ADVANCES IN ATMOSPHERIC SCIENCES, VOL. 38, MARCH 2021, 357–374

• **Review** •

Integrative Monsoon Frontal Rainfall Experiment (IMFRE-I): A Mid-Term Review

Chunguang CUI[1], Xiquan DONG*[2], Bin WANG[1], Baike XI[2], Yi DENG[3], and Yihui DING[4]

[1]*Hubei Key Laboratory for Heavy Rain Monitoring and Warning Research*, *Institute of Heavy Rain*, *China Meteorological Administration*, *Wuhan* 430205, *China*

[2]*Department of Hydrology and Atmospheric Sciences*, *University of Arizona*, *Tucson*, *Arizona* 85721-0011, *USA*

[3]*School of Earth and Atmospheric Sciences*, *Georgia Institute of Technology*, *Atlanta*, *Georgia* 30332-0340, *USA*

[4]*National Climate Center*, *China Meteorological Administration*, *Beijing* 100081, *China*

(Received 17 July 2020; revised 15 October 2020; accepted 2 November 2020)

ABSTRACT

The mei-yu season, typically occurring from mid-June to mid-July, on average, contributes to 32% of the annual precipitation over the Yangtze–Huai River Valley (YHRV) and represents one of the three heavy-rainfall periods in China. Here, we briefly review the large-scale background, synoptic pattern, moisture transport, and cloud and precipitation characteristics of the mei-yu frontal systems in the context of the ongoing Integrative Monsoon Frontal Rainfall Experiment (IMFRE) field campaign. Phase one of the campaign, IMFRE-I, was conducted from 10 June to 10 July 2018 in the middle reaches of the YHRV. Led by the Wuhan Institute of Heavy Rain (IHR) with primary support from the National Natural Science Foundation of China, IMFRE-I maximizes the use of our observational capacity enabled by a suite of ground-based and remote sensing instruments, most notably the IHR Mesoscale Heavy Rainfall Observing System (MHROS), including different wavelengths of radars, microwave radiometers, and disdrometers. The KA350 (Shanxi King-Air) aircraft participating in the campaign is equipped with Ka-band cloud radar and different probes. The comprehensive datasets from both the MHROS and aircraft instruments are combined with available satellite observations and model simulations to answer the three scientific questions of IMFRE-I. Some highlights from a previously published special issue are included in this review, and we also briefly introduce the IMFRE-II field campaign, conducted during June–July 2020, where the focus was on the spatiotemporal evolutions of the mei-yu frontal systems over the middle and lower reaches of the YHRV.

Key words: mei-yu frontal system, IMFRE-I, IMFRE-II

Citation: Cui, C. G., X. Q. Dong, B. Wang, B. K. Xi, Y. Deng, and Y. H. Ding, 2021: Integrative Monsoon Frontal Rainfall Experiment (IMFRE-I): A mid-term review. *Adv. Atmos. Sci.*, **38**(3), 357−374, https://doi.org/10.1007/s00376-020-0209-1.

Article Highlights:

- Brief review of the large-scale background, synoptic pattern, and moisture transport of the mei-yu frontal systems.
- Summary of the important findings from aircraft, surface and satellite observations during IMFRE-I.
- Brief introduction to the motivation and goals of IMFRE-II conducted in summer 2020.

1. Background of the mei-yu frontal systems over the Yangtze–Huai River Valley

The mei-yu season, as it is known in China, or baiu as it is known in Japan, is a specific period of the East Asian summer monsoon that produces most of the summer rainfall from the Yangtze–Huai River Valley (YHRV) in central China to Japan via a quasi-stationary elongated rainband in mid-June to mid-July (Ninomiya and Murakami, 1987; Tao and Chen, 1987; Ding and Chan, 2005; Ding et al., 2007, 2020; Sampe and Xie, 2010; Geng, 2014). The mei-yu season is one of the three heavy-rainfall periods over China (Ding, 1992; Zhang et al., 2006; Luo et al., 2014; Cui et al., 2015), and the mei-yu frontal heavy rainfall contributes a significant portion of the total precipitation in central China (Ding, 1992; Zhang et al., 2006). For example, the mei-yu frontal rainfall, on average, can contribute ~32% of the annual rainfall of Hubei Province in central China (Fang et al., 2019), and up to 50% in some years (Liu and Wang, 2006).

* Corresponding author: Xiquan DONG
Email: xdong@arizona.edu

Hu et al. (2019a) objectively identified three canonical synoptic patterns driving the extreme mei-yu rainfall events during recent decades, the main feature of which is strengthened southerly flow encountering anomalous northerly flow. The southwesterly anomalies are generally associated with the expansion of the western Pacific subtropical high (WPSH), while the anomalous northerlies are driven by several distinct mid–high-latitude disturbances (Fig. 1). The impacts of these synoptic patterns on extreme rainfall are largely realized through anomalous moisture convergence, which is captured by only a subset of global climate models (Hu et al., 2019b). Yang et al. (2019) highlighted the role of moisture transport for the rainstorms over the middle and lower reaches of the YHRV during the mei-yu season. Based on trajectory analysis, they concluded that the main moisture source for heavy rainfall over the YHRV is the Indian Ocean, contributing over 40% of the total water vapor.

At the meso scale of a few hundreds of kilometers, the low-level jet (LLJ; wind speed greater than 12 m s^{-1} at 850 or 700 hPa) to the south of the mei-yu front plays a crucial role in moisture transport and mei-yu rainfall formation (Lin et al., 1992; Cui et al., 2015; Wang et al., 2019). It generally manifests itself as a region of strong southwesterly winds centered at 950 hPa, transporting huge amounts of warm and moist air from the South China Sea and Southwest China (Fig. 2a) to the middle and lower reaches of the YHRV and causes significant moisture convergence there (Cui et al., 2015; Wang et al., 2019; Cui et al., 2020a). When these warm, moist air masses mix with the south-

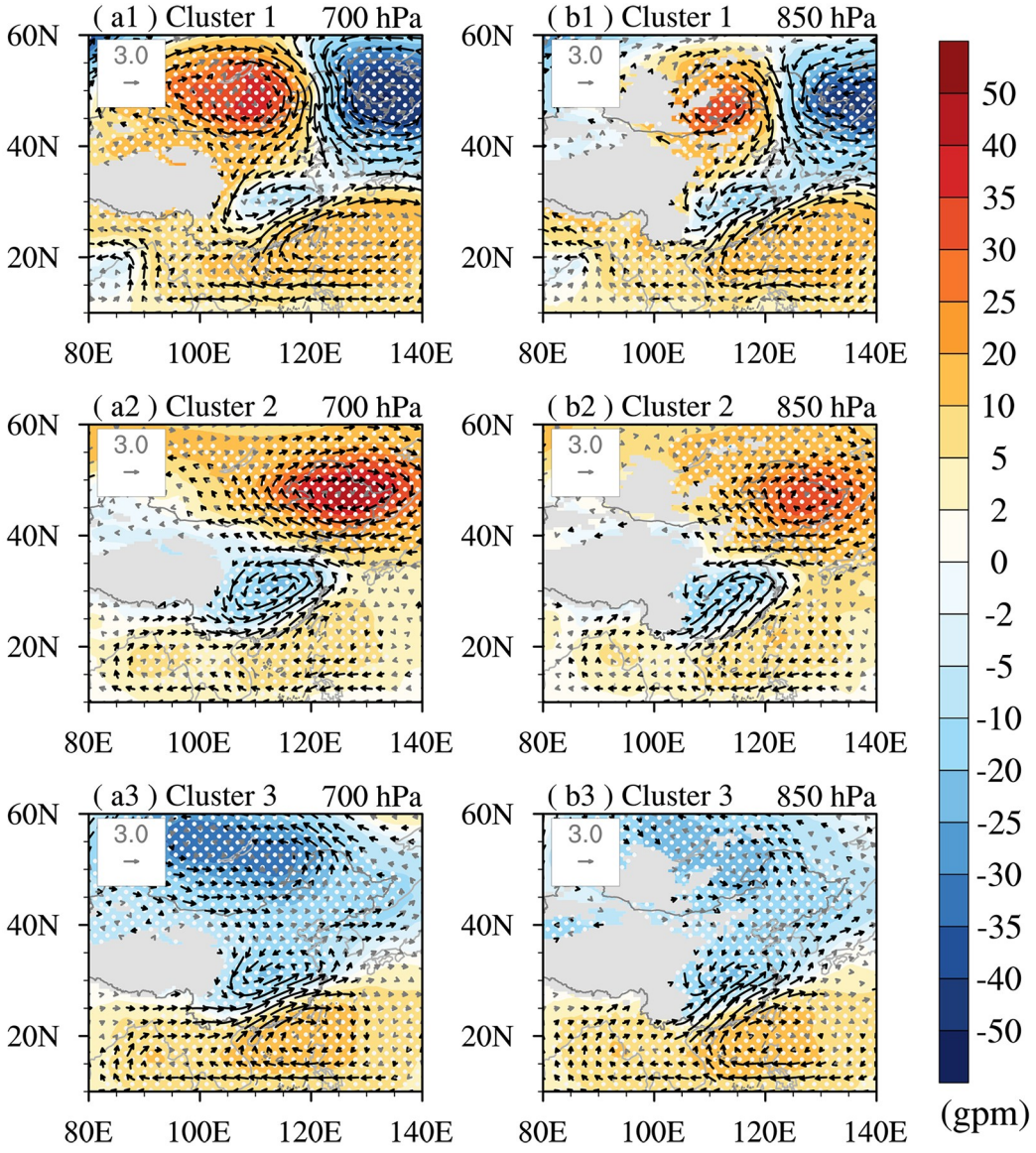

Fig. 1. The three typical synoptic patterns driving the extreme mei-yu rainfall, represented by the mean anomalies of geopotential height (units: gpm) and wind vectors (units: m s^{-1}) at (a) 700 hPa and (b) 850 hPa. The geopotential height (wind vectors) anomalies that are statistically significant at the 0.1 level are indicated by dotted areas (black vectors) [reproduced from Hu et al. (2019a)].

ward invasion of cold and dry air masses from the north over the YHRV, heavy precipitation events are likely to occur (Fig. 2b). Statistics reveal that 79% of LLJs are accompanied by rainstorms during the mei-yu period, while 83% of the rainstorms are accompanied by LLJs (Cui et al., 2020b; Wang et al., 2000).

In addition to LLJs, the WPSH also plays an important role in the variability of rainstorms within the YHRV, as discussed in Wang et al. (2019) and Hu et al. (2019b). Some studies have noted the influence of the South Asian high (SAH) and upper-level jets (ULJs) and their interactions with other systems, as both the eastward expansion of the SAH and the intensification of ULJs could provide additional forcing for rising motion (Chen and Zhai, 2014, 2016; Hu et al., 2019a, Yang et al., 2019). Figure 1b shows a mei-yu rainband, which includes multiscale convective systems, such as meso-β-scale (20–200 km) and meso-γ-scale (2–20 km) systems. These two systems are key direct factors in generating heavy precipitation during the mei-yu period (Ninomiya and Kurihara, 1987), and ~60%–70% of mei-yu precipitation can be associated with the meso-β-scale convective systems (Zhang et al., 2002, 2004).

The climatological mean of annual mei-yu rainfall over Hubei Province during the period 1951–2019 is 245.6 mm (Fig. 3). However, there is substantial interannual variability. For example, the annual mei-yu rainfall amounts in the years 1958, 1963, 1965, 2001 and 2005 were only ~20% of the climatological mean, whereas those in the years 1954, 1969, 1980, 1983, 1992, 1996, 1998 and 2016 were more than double the climatological mean. The total mei-yu rainfall in 2018 was 174.6 mm, which is below the climatological mean. The 2018 mei-yu period was characterized by short and light precipitation with a few localized heavy rainfall events. Therefore, the year 2018 was not a typical mei-yu season.

Cui et al. (2020b) analyzed the spatial distributions of

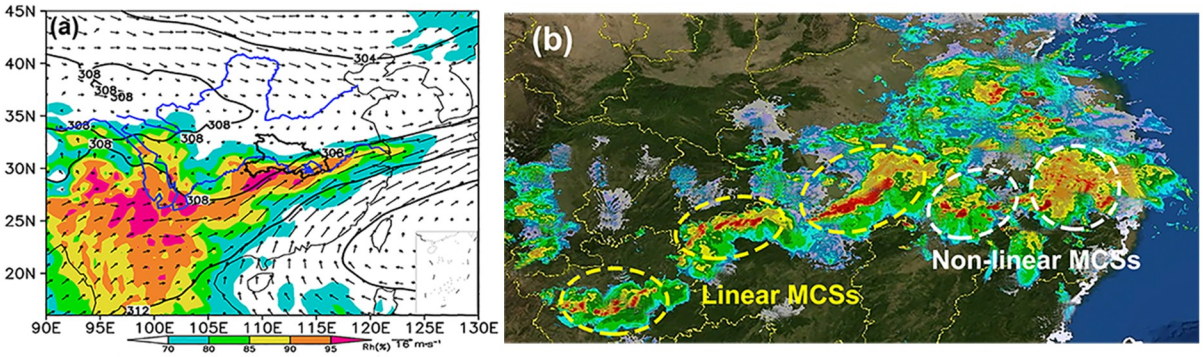

Fig. 2. (a) Synoptic systems at 700 hPa generated from NCEP reanalysis data during the mei-yu season in 1991, including geopotential height (black contours; units: dagpm), wind field (vectors; units: m s^{-1}), and relative humidity (color-shaded; units: %), in eastern Asia. The blue lines represent the Yangtze and Yellow rivers, and the blue triangle is the location of Xianning site (29.51°N, 114.22°E) in southeastern Hubei Province (black line), central China. The Xianning site is the central facility of the China Meteorological Administration's Institute of Heavy Rain (IHR) Mesoscale Heavy Rainfall Observing System (MHROS) [reproduced from Cui et al. (2015)]. (b) Radar composite image.

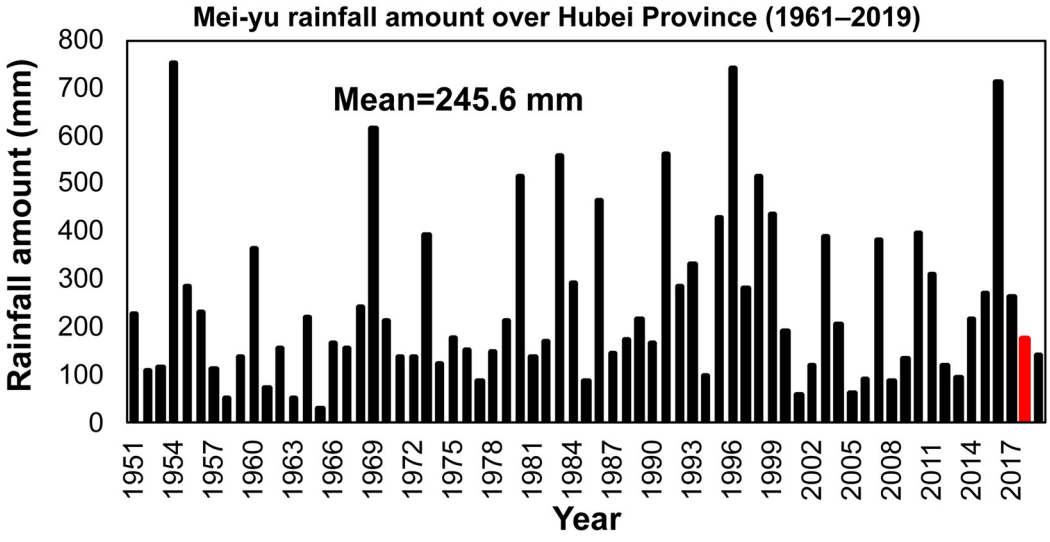

Fig. 3. Climatology of The annual mei-yu rainfall during the period 1951–2019. The red color represents the rainfall in 2018.

the total rainfall amount (Fig. 4a) during the mei-yu period from all precipitating systems (Figs. 4b and d) and only from mesoscale convective systems (MCSs) (Figs. 4c and e) over the YHRV and southern China regions, during the period 2014–18. They concluded that the mei-yu MCSs contribute 20% to 60% of the total precipitation during the mei-yu period, and the regional contribution could be greater than 90%. The mean MCSs' accumulated precipitation values over the YHRV and southern China during the mei-yu season for the 5-yr period are 59.2 mm and 66.6 mm, respectively, which contribute 34.9% and 28.2% to all mei-yu precipitation, primarily due to higher convective available potential energy over southern China (976.2 J kg^{-1}) than over the YHRV (786.6 J kg^{-1}).

It is well recognized that the mei-yu frontal rainfall has a pronounced diurnal variation, such as its bimodal distribution and narrow zone. Climatologically, many rainfall systems in the mei-yu frontal zone have a major peak in the morning, and some systems have an afternoon-peak feature. The nocturnal variation of mei-yu rainfall systems tends to take place in a very narrow zone over the YHRV, which is significantly different to the adjacent south and north regions with afternoon-peak rainfall (e.g., Geng and Yamada, 2007; Guan et al., 2020). The results of Zhang et al. (2020) reveal that for typical mei-yu years, precipitation has a single morning peak (0930 LST), which is induced by strong southwesterly moisture transport. However, during atypical mei-yu years, the diurnal variation in precipitation appears as a bimodal structure with peaks in the early morning (0630 LST) and afternoon (1600 LST), where the morning peak is related to the low-level water vapor flux, but weaker than normal mei-yu years (Fig. 5), and the afternoon peak is related to the local solar heating. The diurnal variations of MCSs' precipitation along the mei-yu frontal system have also been investigated in the study of Cui et al. (2020b). The MCSs occurring in southern China and the Yangtze River basin were studied separately. Although the diurnal variabilities of MCSs' precipitation in these two regions have some differences, morning precipitation amount maxima are found in both regions, which is associated with the enhanced nocturnal LLJ. The enhanced nocturnal LLJ creates more favorable thermodynamic conditions for triggering convection

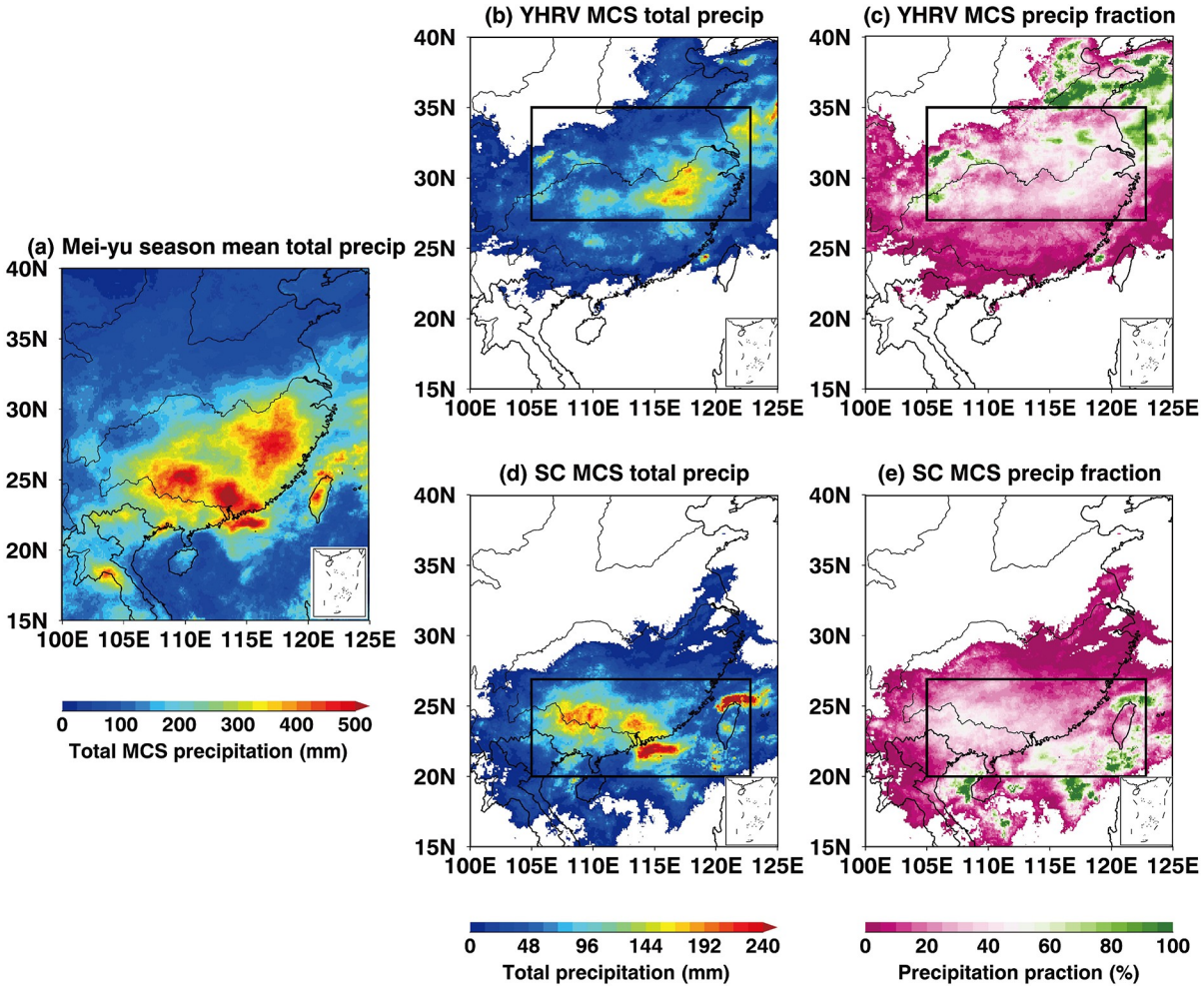

Fig. 4. (a) Spatial distribution of 5-year mean total mei-yu season precipitation from all systems. (b, d) Total precipitation from MCSs, and (c, e) the contribution of mei-yu precipitation to all precipitation for the YHRV and southern China domains [reproduced from Cui et al. (2020b)].

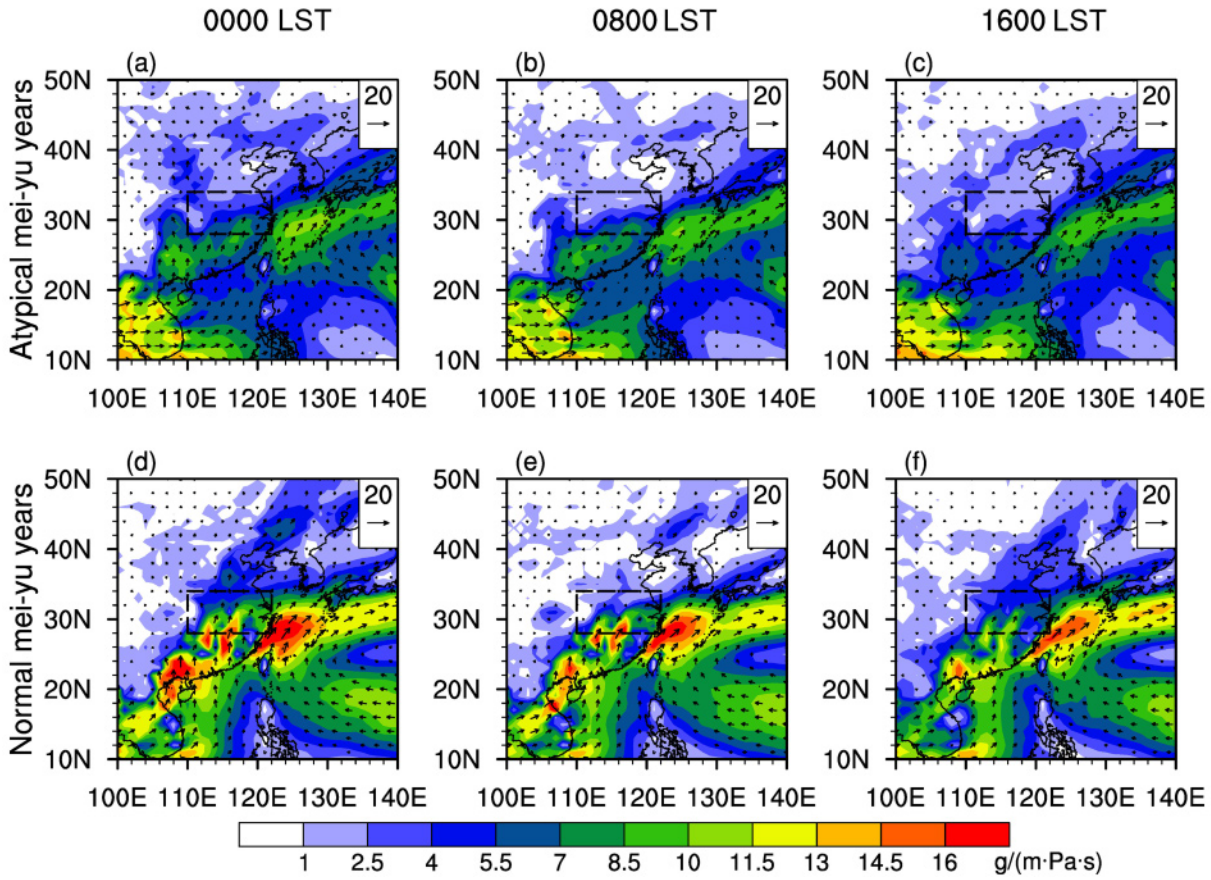

Fig. 5. Average distribution of the 850-hPa water vapor flux at different local times during the mei-yu periods in (a–c) atypical mei-yu years and (d–f) normal mei-yu years [reproduced from Zhang et al. (2020)]. The dashed rectangles indicate the location of the middle and lower valley of the Yangtze River.

overnight. The results from this study indicate that the diurnal variation of precipitation associated with convective systems are regionally dependent, but are still determined by the large-scale environmental conditions.

During phase one of the Integrative Monsoon Frontal Rainfall Experiment (IMFRE-I), there were a few moderate rainfall events and one severe thunderstorm on 30 June 2018 over the Xianning site. In this mid-term review, we focus on discussing the observational results during IMFRE-I, particularly for the 30 June event, in the following sections. Some modeling efforts (e.g., Li et al. 2020; Liu et al. 2020) regarding the effects of aerosols on the cloud properties along the mei-yu frontal system and the microphysical processes responsible for mei-yu heavy precipitation will not be included in this mid-term review.

The rest of the paper is organized as follows: Section 2 briefly describes the motivation and goals of IMFRE. Section 3 highlights the important findings from multiple platforms during IMFRE-I. Finally, IMFRE-II, conducted during summer 2020, is briefly introduced in section 4.

2. Motivation and design of IMFRE

To better understand the dynamic and physical processes of mei-yu frontal rainfall, the IMFRE-I field campaign was conducted from 10 June to 10 July 2018 in the middle reaches of the YHRV, a region strongly affected by the East Asian summer monsoon. The experiment was organized by the Wuhan Institute of Heavy Rain (IHR), China Meteorological Administration, with primary support from the National Natural Science Foundation of China. The multiscale mei-yu frontal system is responsible for most of the heavy rainfall and flooding events in central China during the boreal warm season, yet observations are seriously lacking for a system of such tremendous scientific and societal importance. To address these critical needs and provide an observational basis for understanding, modeling and predicting the mei-yu frontal systems, the IMFRE-I field campaign was designed in order to lay out the foundation for integrative ground-, satellite-based and aircraft in-situ measurements and monitoring of the mei-yu frontal systems. This field campaign was the first attempt at collecting comprehensive datasets during the mei-yu period over the middle reaches of the YHRV in central China. No attempt has been made to provide an exhaustive climatological dataset of mei-yu frontal systems; rather, the emphasis of IMFRE-I was to provide synthetic datasets. Through an integrative analysis of comprehensive datasets and mesoscale modeling

efforts, we can partially answer the posed scientific questions from IMFRE-I.

A special focus is placed upon the dynamic and thermodynamic structures of the mesoscale systems embedded in the mei-yu frontal system with their associated cloud properties and precipitation processes. The ground-based observations include those obtained from the IHR Mesoscale Heavy Rainfall Observing System (MHROS; Cui et al., 2015), regular soundings and surface meteorological variables, located at the Xianning surface site (Fig. 6). IHR-MHROS consists of mobile C-band and X-band polarimetric precipitation radars (C-POL and X-POL), millimeter wavelength cloud radars (MMCR), fixed S-band precipitation radars, micro rain radars (MRR), a GPS network, microwave radiometers (MWR), radiosonde soundings, wind profiler radars (WPR), and Parsivel and 2D video (2DVD) disdrometers. In addition to the Ka-band cloud radar, the Shanxi King-Air (KA350) aircraft participating in the campaign is equipped with the following sensors: a cloud droplet probe (CDP), cloud imaging probe (CIP), precipitation imaging probe (PIP), passive cavity aerosol spectrometer probe (PCASP), cloud condensation nuclei counter (CCN-200), and total water content/liquid water content sensors (TWC/LWC) (Yang et al., 2020), and flew ~25 hours during IMFRE-I, based at the Yichang airport (Fig. 6; ~300 km west of the Xianning site). Table 1 lists all ground-based instruments and aircraft probes, as well as their observational ranges and resolutions during IMFRE-I. Multiple satellite observations and retrievals were collected and processed, including data from the Global Precipitation Measurement Mission Dual-Frequency Precipitation Radar (GPM-DPR) and Integrated Multi-satellite Retrievals (IMERG), Chinese Fengyun and Japanese Himawari-8 (Cui et al., 2020b; Sun et al., 2020). Through building synthetic datasets and mesoscale modeling analysis during IMFRE, we aim to answer the following questions:

(1) Can we gain more insight into the raindrop formation and growth processes at different stages (developing, mature, dissipating) of the mei-yu stratiform and convective rain systems, the impacts of moisture sources on MCS formation, and cloud and precipitation microphysical properties?

(2) What are the dynamic and thermodynamic mechanisms driving the lifecycle characteristics of MCSs and the mei-yu frontal systems, as well as their associated cloud and precipitation properties?

(3) How can we evaluate the different microphysics schemes in the WRF model and find the best solution of quantitative precipitation forecasting for the middle reaches of the YHRV?

The unique feature of the IHR MHROS is to provide continuous, high temporal, spatial and vertical resolutions of observations from multiple sensors, particularly during the mei-yu seasons. Figure 7 shows a few photos during IMFRE-I and Figs. 8–19 illustrate the comprehensive observations from a suite of remote sensors of the IHR MHROS, as well as radar mosaic and satellite observations used during an event that occurred on 30 June 2018 during IMFRE-I as an example. The rainfall event on 30 June 2018 was the only severe thunderstorm observed at the Xianning site dur-

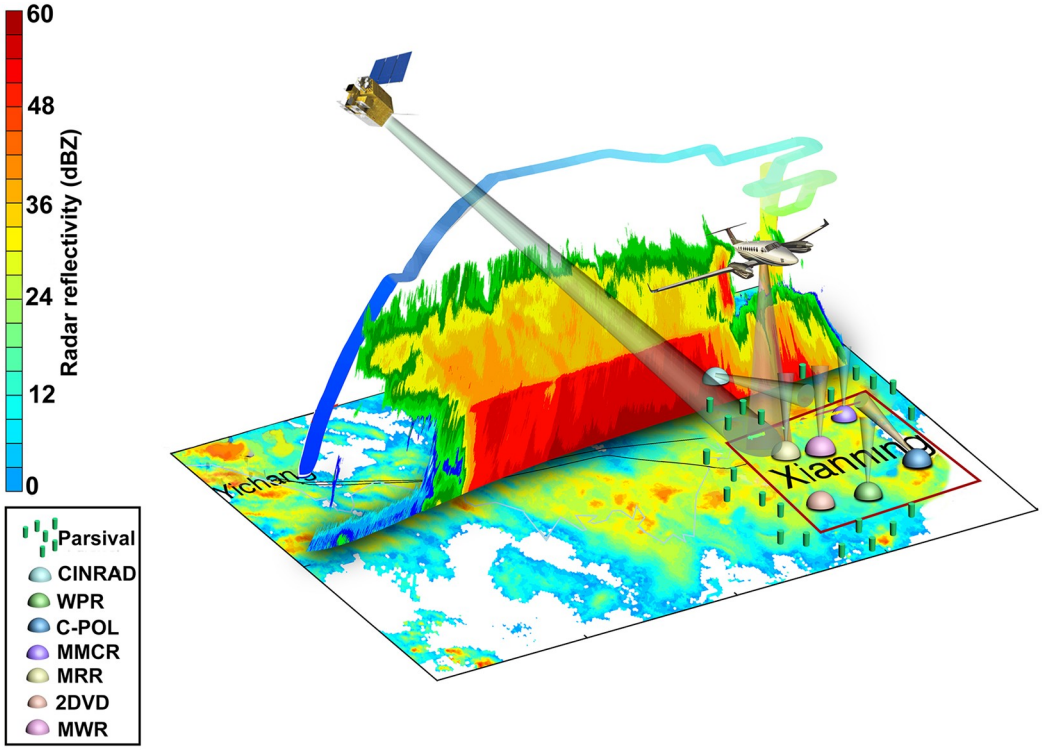

Fig. 6. 3D structure of surface-site, satellite and aircraft observations during the IMFRE-I field campaign in June–July 2018 over Hubei Province, central China.

Table 1. List of ground-based and airborne instruments used in IMFRE-I.

Location	Instruments	Observed variables	Range	Resolution
Ground-based	C-band Polarimetric radar	Z, V, W, Z_{DR}, Φ_{DP}, ρ_{HV}	150 km	150 m and 6 min
	Microwave radiometer	Cloud LWP and PWV	10 km	50–200 m and 2 min
	Millimeter cloud radar	Z, V, W, LDR	30 km	10 m and 5 s
	Micro rain radar	Profiles of raindrop spectrum, terminal velocity, intensity	3 km	100 m and 1 min
	2D video disdrometer	Raindrop spectrum, falling speed, shape, rain intensity	–	1 min
	Tropospheric wind profiler radar	Horizontal wind speed and direction, vertical wind velocity, C_n^2 profile	0–16 km	120–480 m
	Laser ceilometer	Cloud base height	0~15 km	–
Airborne	Cloud droplet probe	Droplet spectrum	2–50 μm	40 bins and 1 s
	Cloud imaging probe	Droplet spectrum	12.5 μm–1.55 mm	25 μm and 1 s
	Precipitation imaging probe	Particle spectrum	100 μm–6.2 mm	100 μm and 1s
	Passive cavity aerosol spectrometer probe	Number concentration	0.1–3 μm	1 s
	Cloud condensation nuclei counter	Particle size, Number concentration	0.75–10 μm	1 s
	Total water content/liquid water content sensors	Liquid water content	0–10 g m^{-3}	1 s

Note: that Z = reflectivity factor; V = Doppler radial velocity; W = Doppler spectrum width; Z_{DR} = differential reflectivity; Φ_{DP} = differential phase shift; ρ_{HV} = correlation coefficient; LDR = linear depolarization ratio; C_n^2 = structure constant of atmospheric refractive index; LWP = liquid water path; PWV = precipitable water vapor.

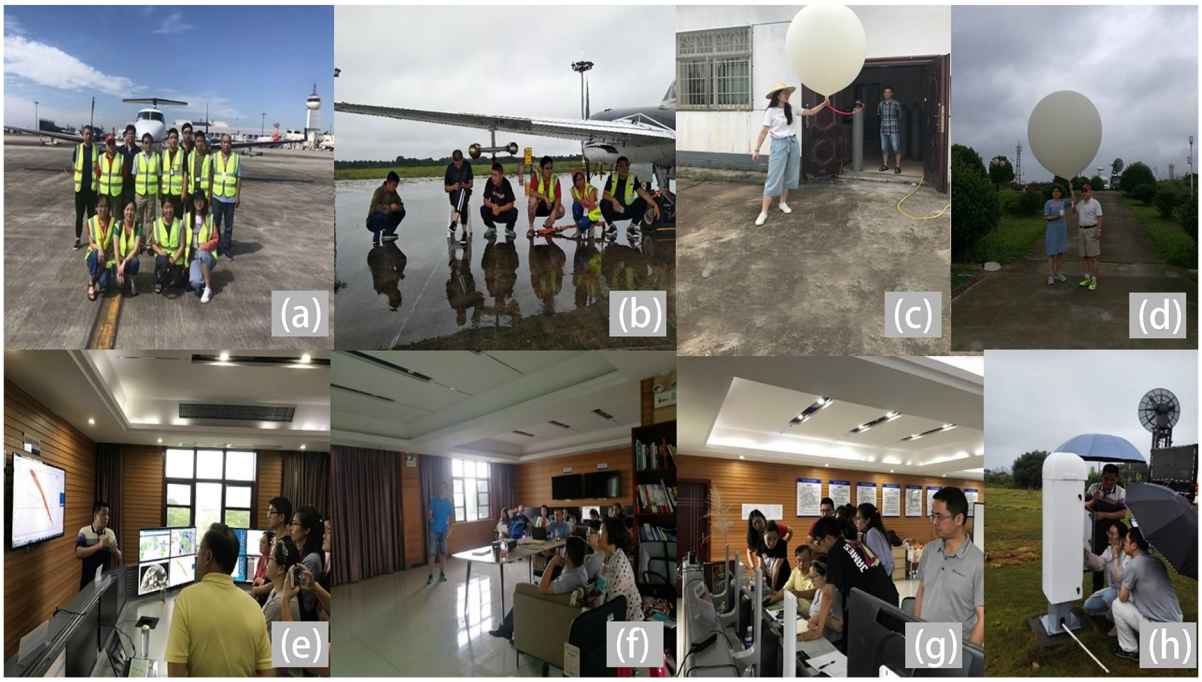

Fig. 7. (a) The Shanxi Aircraft crew with the IMFRE-I leadership team. (b) Waiting for permission to take off on 30 June 2018. (c) Filling the balloon. (d) Launching the balloon. (e) Weather forecasting. (f) Daily meeting regarding observational results. (g) Discussion meeting. (h) Troubleshooting the MRR.

ing IMFRE-I. This system (and water vapor) was advected from northwestern Hubei Province, initiated in the early morning over Hubei Province, developed before 1100 LST, then became mature from 1100 LST to 1600 LST, and finally dissipated (or moved out) after 1600 LST (Fig. 8).

The vertical distributions of the system were observed by precipitation radar (reconstructed S-band radar reflectivity over the Xianning site), MMCR and MRR, as well as the surface rainfall amount at the Xianning site. The S-band radar reflectivity (Fig. 9a) and radar mosaic (Figs. 8d–f) illustrate that the radar reflectivity became greater and greater from early morning to noon, and the system started to dissip-

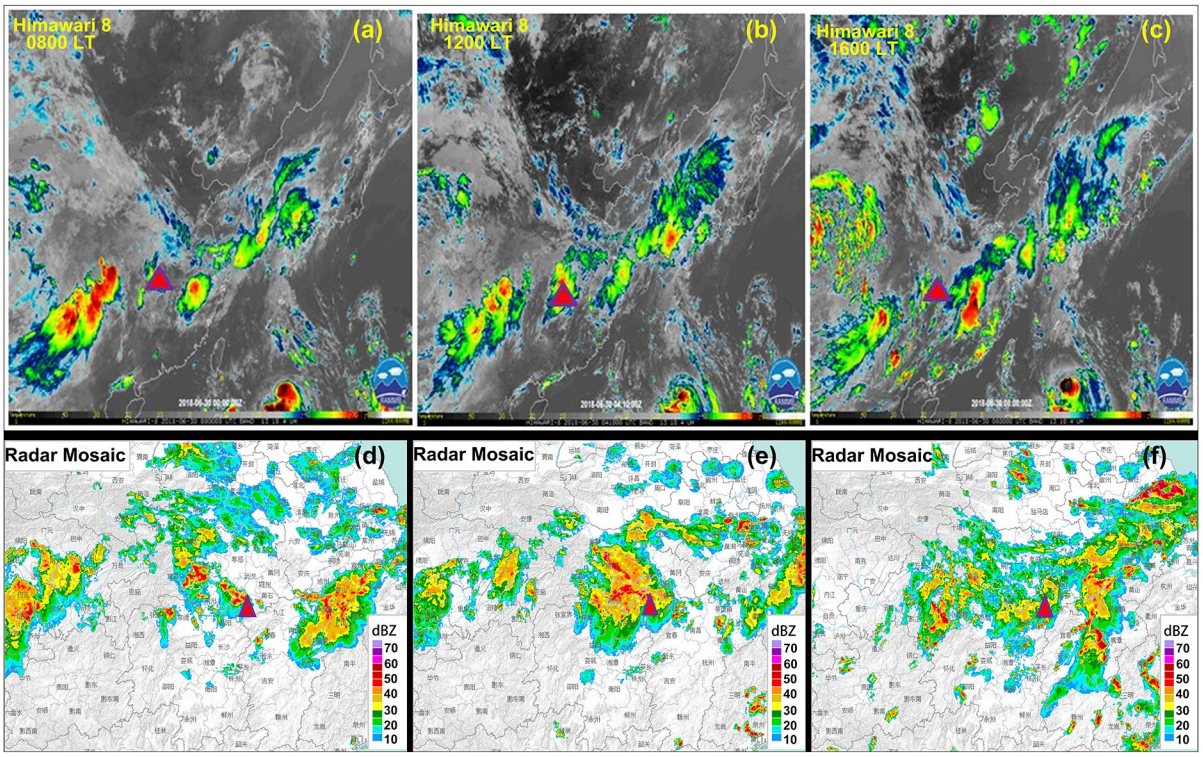

Fig. 8. (a–c) Himawari brightness temperatures at wavelength λ = 10.4 μm, ranging from T = −8°C (red) to 40°C (black); and (d–f) radar mosaic composite images at 0800 (a, d), 1200 (b, e) and 1600 (c, f) LST 30 June 2018. The triangle represents the Xianning surface site. Note that different grid boxes are used for satellite and radar images.

ate after 1700 LST over the Xianning site. The cloud radar was not turned on before noon due to a severe thunderstorm and lightning, and the cloud and precipitation properties below 3 km were derived by MRR with a 100-m vertical resolution, a great addition to the S-band and cloud radar observations. The much higher MRR reflectivity measurements near the surface during the period 0900–1200 LST in Fig. 9c correlate well with the surface rainfall measurements (Fig. 9d). The KA350 aircraft was not allowed to take off due to air control until 1700 LST, and flew over the Xianning site at around 1830 LST. The vertical distributions of atmospheric temperature, relative humidity, water vapor density and LWC retrieved from the MWR over the Xianning site are shown in Fig. 10. The high water vapor density and LWC during the period 0900–1200 LST, although their vertical distributions need to be further validated, strongly correlate with the S-band and MRR reflectivity measurements. To provide more information, the profiles of atmospheric temperature, dewpoint temperature, and mixing ratio observed by GPS radiosonde soundings on 30 June (morning and afternoon) and 17 and 18 June are plotted in Fig. 11. Figures 8–11 demonstrate that it is crucial to have different remote sensors, including both active and passive, as well as surface rainfall and raindrop size distribution measurements, to observe the MCSs in order to have a complete horizontal and vertical distribution of the system due to their different sensitivities. These observations are needed to investigate the formation mechanisms and spatiotemporal evolutions of MCSs and mei-yu frontal systems.

3. Highlights from IMFRE-I

Figures 12–19 have been selected from the recently published papers from the Journal of Geophysical Research-Atmospheres IMFRE special issue to represent the observational results from ground-based remote sensors (Fu et al., 2020; Zhou et al., 2020), satellites (Sun et al., 2020), and aircraft (Yang et al., 2020), as well as the newly developed parameterizations from these new results (Fu et al., 2020; Zhou et al., 2020). These results can be used to partially answer the proposed three scientific questions for IMFRE-I.

3.1. *Raindrop size distributions from MRR, 2DVD and GPM-DPR*

The MRR, a 24 GHz K-band frequency-modulated, continuous-wave Doppler radar, can estimate the profiles of raindrop size distributions (DSDs) converted by power spectra and terminal fall velocities at different heights under certain assumptions. A total of 1896 1-min rain samples observed by MRR during IMFRE-I were collected and classified into three categories of convective rain (CR), stratiform rain (SR), and light rain (LR) to study the vertical structures of rain DSDs as shown in Fig. 12. The LR category is dominated by the evaporation process of smaller raindrops above 1 km with some evidence for the decreased lg$N(D)$ for D < 0.4 μm, and the breakup processes of larger raindrops below 1 km with the sharply decreased $N(D)$ of

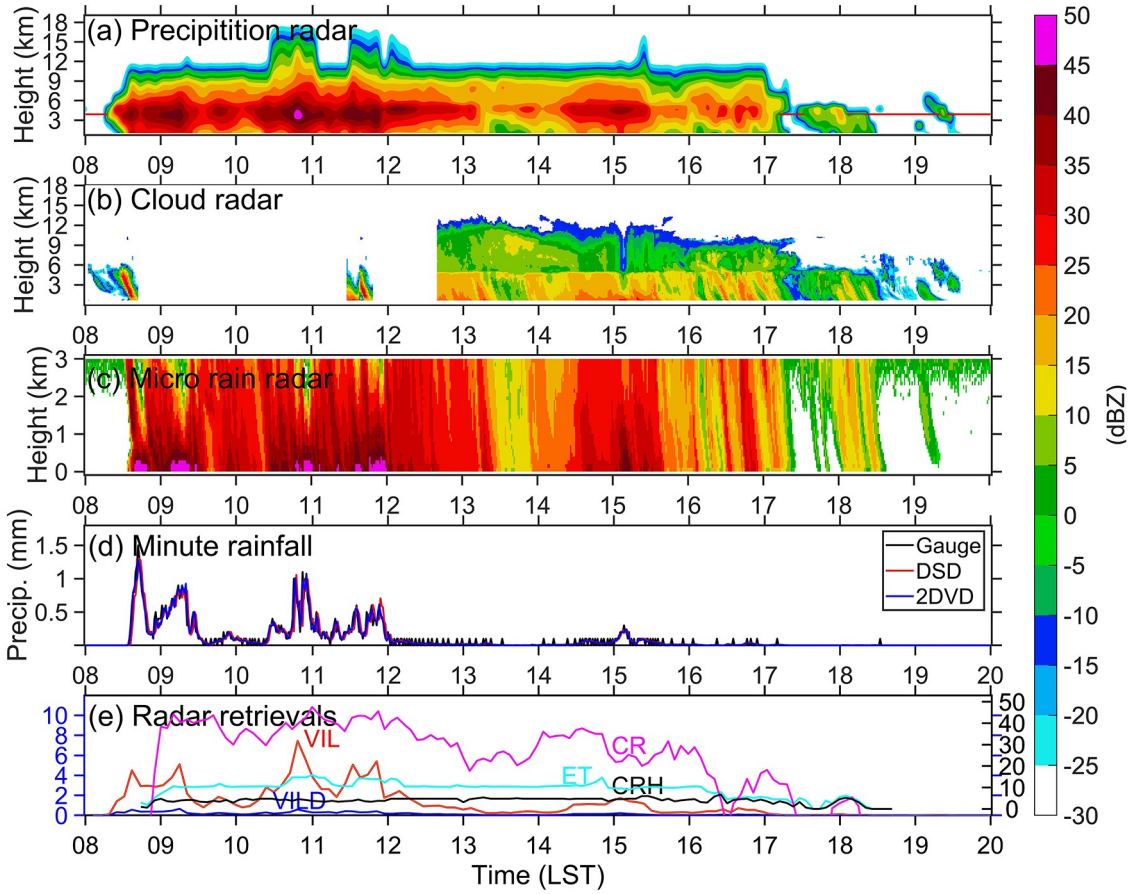

Fig. 9. Observations from three radars during IMFRE-Ⅰ, including the (a) S-band precipitation radar, (b) 35-GHz cloud radar, and (c) 24-GHz MRR. (d) Rain rates from the Parsival disdrometer (DSD), 2D video disdrometer (2DVD), and tipping bucket gauge. (e) Retrieval products from the S-band precipitation radar (VIL: vertically integrated liquid water content; VILD: vertically integrated liquid water content density; CRH: composite reflectivity height; ET: echo top height; CR: composite reflectivity) as part of the Institute of Heavy Rain (IHR) Mesoscale Heavy Rainfall Observing System (MHROS) over the Xianning surface site on 30 June 2018.

medium-sized (0.4 mm < D < 1.5 mm) and large-sized raindrops (D >1.5 mm). The CR category is dominated by the coalescence process. The raindrops above 1 km with slightly increased lg$N(D)$ for all of the detected raindrops indicate the collecting process with undetected cloud droplets, whereas the raindrops below 1 km with the increased lg$N(D)$ for the D > 1.0 μm and the decreased lg$N(D)$ for the D < 0.6 μm indicate that significant growth via the coalescence process occurs only when small and medium-sized raindrops are collected by large raindrops. The variations in vertical distributions of the DSDs for LR, SR, and CR can be attributed to different formation and dissipation processes of the raindrops. These results can help in improving the understanding of the physical processes for different rain types, as well as their vertical variations, and will shed light on improving the rain microphysical parameterizations for model simulations and predictions.

Figure 13 shows the spatial distributions of column maximum reflectivities by the GPM-DPR and corresponding brightness temperatures observed by the FY-2G/FY-2E satellites for the three selected cases to represent the developing, mature and dissipating stages of precipitation systems during IMFRE-1 (Sun et al., 2020). Figure 14 presents the types (CR and SR) and three stages (developing, mature and dissipating) of all mei-yu precipitation systems collected and processed during the period 2016–18 in the study of Sun et al. (2020). In general, the coalescence process overwhelms the evaporation and/or breakup processes in the SR developing and mature stages, which results in increased radar reflectivity (Z) and rain rate (RR) values below the bright bands toward the surface. However, none of the processes is dominant in the SR dissipating stage. For CR, coalescence is the dominant process for the three stages.

The PARSIVEL disdrometer–measured RR, Z, raindrop diameter (D_m) and lgN_w during IMFRE-I were used to validate the GPM-DPR–retrieved near-surface rain and DSDs for the first time in central China and showed good agreement (Sun et al., 2020). The histograms of D_m and lgN_w for all samples, CR, and SR during the 2016–18 mei-yu seasons are shown in Fig. 15 (Fu et al., 2020), where the raindrop D_m and lgN_w values in CR are larger and higher than those in SR. Compared with the results over the lower

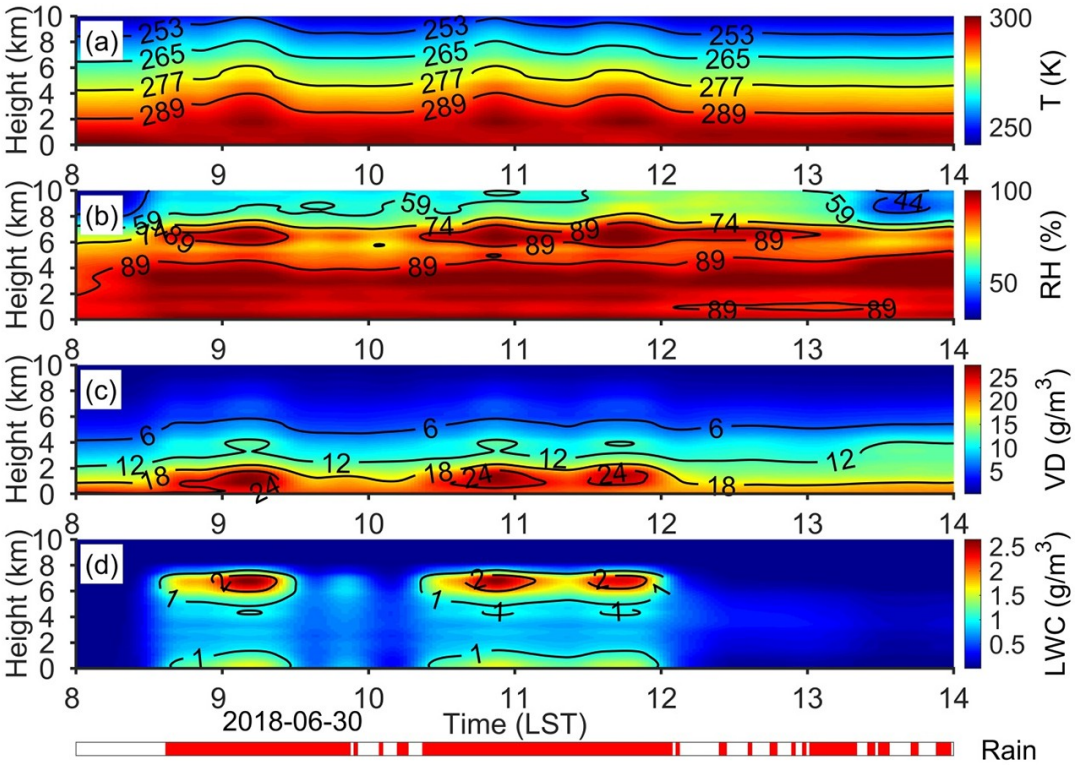

Fig. 10. Vertical distributions of atmospheric (a) temperature, (b) relative humidity, (c) water vapor density, and (d) LWC retrieved from the MWR as part of the Institute of Heavy Rain (IHR) Mesoscale Heavy Rainfall Observing System (MHROS) over the Xianning surface site on 30 June 2018. Horizontal bar indicates the rain condition during measurement, and the red bar and white bar are the period with and without rain, respectively.

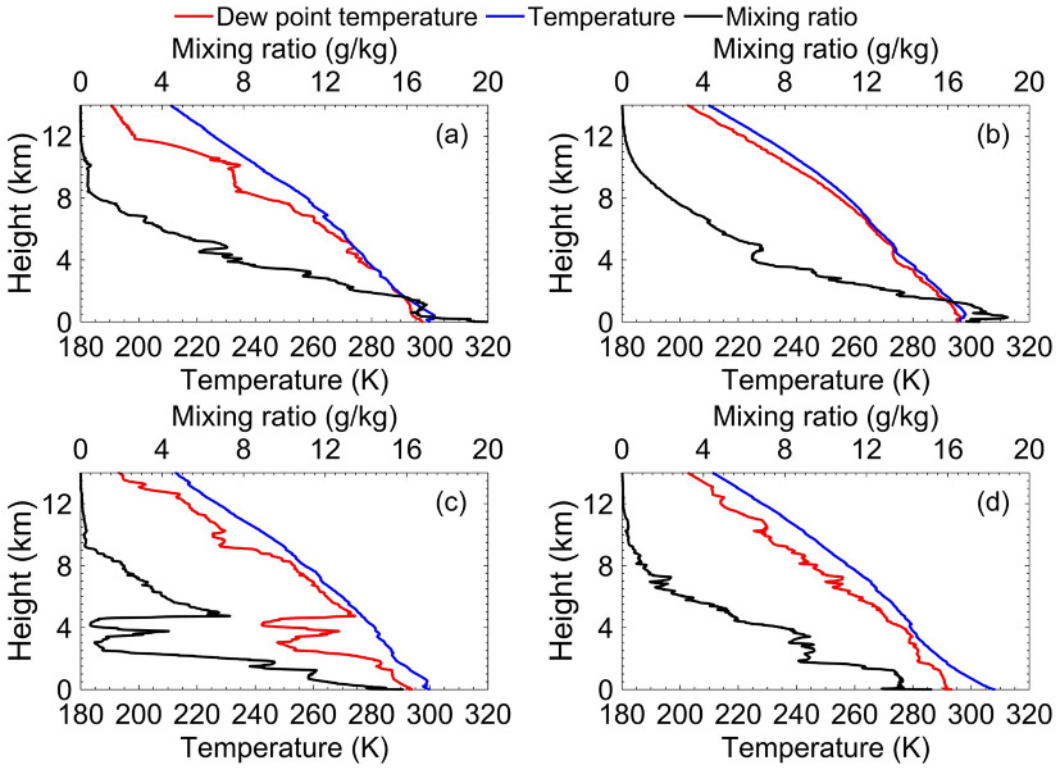

Fig. 11. GPS radiosonde observations at (a) 0800 LST 30 June, (b) 1400 LST 30 June, (c) 0800 LST 17 June, and (d) 1400 LST 18 June 2018. The profiles of temperature (blue) and dewpoint temperature (red) are displayed on the bottom *x*-axis, and the profile of mixing ratio (black) is presented on the top *x*-axis.

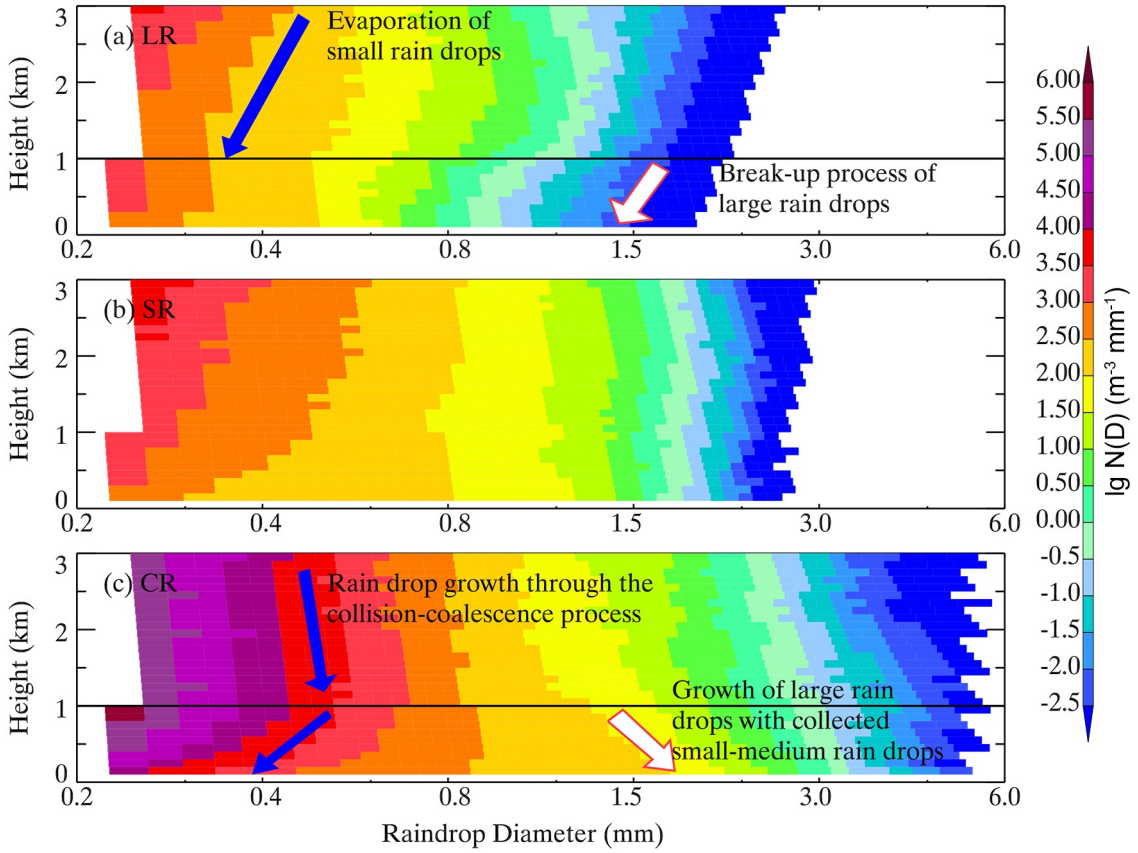

Fig. 12. Vertical distributions of rain DSDs for the classified rain of (a) light rain (LR), (b) stratiform rain (SR), and (c) convective rain (CR) during IMFRE-1 [reproduced and modified from Zhou et al. (2020)].

reaches of the YHRV, the RR and total accumulated rainfall over the middle reaches are greater, especially for heavy rainfall. The SR raindrop size increases with RR over both the middle and lower reaches, whereas the N_w values over the middle reaches are much higher. Opposite to the SR results, the CR raindrops over the middle reaches are larger, while their N_w values are similar to one another.

3.2. *Comparison between aircraft in-situ measurements and ground-based retrievals*

The KA350 aircraft measurements taken within clouds during IMFRE-I can provide a "cloud truth" to validate ground-based observations, classifications and retrievals, which has not been achieved from previous studies. These aircraft measurements, as well as ground-based observations and retrievals, will shed light on the microphysical parameterizations of mei-yu frontal rainfall.

Figure 16a shows reflectivity measurements from the Ka-band radar on the KingAir aircraft on 19 June 2018 during IMFRE-I. The center frequency of Ka-band radar is 35.64 GHz (λ = 8.5 mm) with two transmitters upward and downward, respectively, so it can observe the clouds in two directions. Figure 16b shows the aircraft in-situ measured cloud and drizzle particle size distributions (PSDs) at different altitudes within the cloud layer when the KA350 climbed up from the bottom to top of the cloud layer. The PSDs at the bottom, center and top of the cloud layer demonstrate that the cloud-droplet number concentration (and cloud liquid water content) increases but particle size decreases with height; that is, there is a large amount of small-sized cloud droplets near the cloud top, while a few large-sized drizzle drops exist near the cloud base.

The hydrometeor classifications (HCs) derived from IHR C-POL polarimetric variables are validated by the KA350 PIP measurements during IMFRE-I (Fig. 17). The identification of ice particles by C-POL (Fig. 17c), except for graupel owing to the similar polarimetric characteristics with snow in anvil clouds, is basically consistent with the in-situ aircraft PIP measurements (Fig. 17d). This preliminary validation using in-situ PIP measurements suggests that the C-POL HC results are reasonable; however, more evaluations are needed to improve the performance of the HC algorithm for mei-yu frontal rainfall systems. To the best of our knowledge, this work is the first time that C-POL-classified hydrometeors have been validated against aircraft in-situ measurements over the middle reaches of the YHRV, which will pave the way for future studies related to mei-yu frontal rainfall systems.

3.3. *Development of precipitation parameterizations*

The power-law relationship of radar reflectivity (Z) and rain rate (R), $Z = aR^b$, is widely used in radar QPE (quantitative precipitation estimation). The coefficient a and exponent b depend on the climate, precipitation type, and geo-

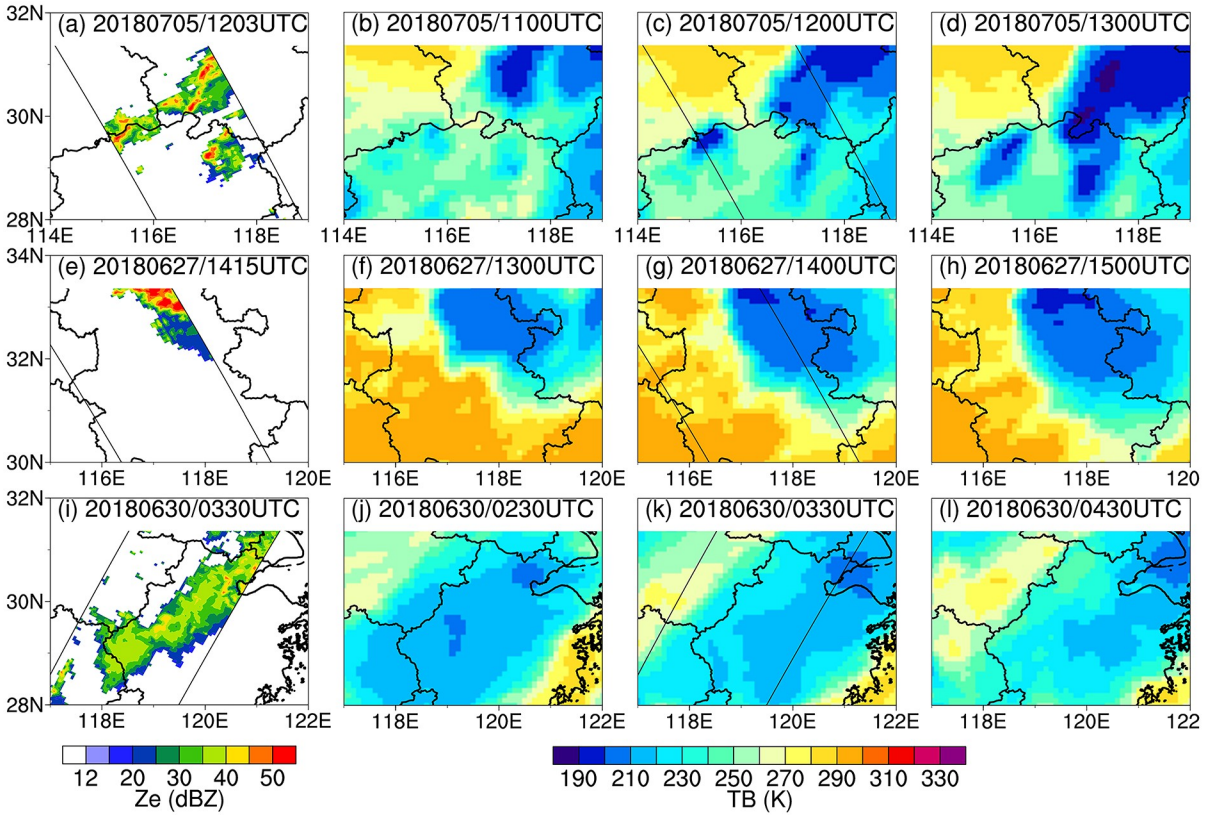

Fig. 13. (a, e, i) Spatial distributions of column maximum reflectivities measured by the GPM-DPR instrument for the three selected cases during IMFRE-1. (b–d, f–h, j–l) The corresponding brightness temperatures observed by FY-2G/FY-2E satellites from one hour before to one hour after the occurrence (within ±1 h) of precipitation in the (a–d) developing stage, (e–h) mature stage, and (i–l) dissipating stage. The diagonal lines represent the edges of the DPR swaths [reproduced from Sun et al. (2020)].

graphical location. Figure 18 shows scatterplots of Z–R values and the least-squares fitted power-law Z–R relation for CR during the 2016–18 mei-yu seasons (Fu et al., 2020). The $Z = 300R^{1.4}$ relation is widely used for CR over the continental United States based on NEXRAD reflectivity (Marshall and Palmer, 1948; Fulton et al., 1998). The Z–R relation derived from Fu et al. (2020) is close to the classic NEXRAD Z–R relation, but differs to those derived from the lower reaches of the YHRV (Chen et al., 2013; Jin et al., 2015). For a given radar reflectivity Z, the rainrates (R) in Fu et al. (2020) are lower than those from the lower reaches. The difference in the Z–R relation might be caused by different precipitation microphysical processes.

The coefficient a and exponent b of the Z–R relationship, $Z = aR^b$, are almost exclusively derived from the surface measurements as shown in Fig. 18. Zhou et al. (2020) found that there are different Z–R relationships at different heights for the LR, SR, and CR. Figure 19 shows the vertical distributions of the coefficient a and exponent b of Z–R relationships for the three rain categories derived from the MRR measurements during IMFRE-I. Generally speaking, there is significant vertical variability in both the coefficients and exponents for all three categories, which are dominated by different DSDs and microphysical processes. The height-dependent Z–R relationships found in Zhou et al. (2020) will provide insightful information for operational radar QPE of monsoon frontal rainfall in central China.

4. Future work (IMFRE-II)

The original design of IMFRE mainly focused on the middle reaches of the YHRV, centered at the Xianning surface site. The Shanxi aircraft was based at the Yichang airport during IMFRE-I, which is about 300 km away from the surface site as shown in Fig. 6. This caused some problems regarding the collocation of aircraft in-situ measurements with ground-based observations. First, it normally takes about one hour for the aircraft to fly over the surface site, which severely limits the time of aircraft sampling over the surface site. Second, it is challenging to forecast weather conditions over the regions of Yichang and Xianning that allow the aircraft to take off and perform sampling during a severe thunderstorm. Third, the Xianning surface site is close to Wuhan city, the largest city in the middle reaches of the YHRV. During a severe thunderstorm, many airplanes are delayed for landing or taking off. Therefore, our flight plan was a relatively low priority. The 30 June event is a good example of these issues.

In light of the above reasons and after learning from the successes and mishaps of IMFRE-I, we decided to build

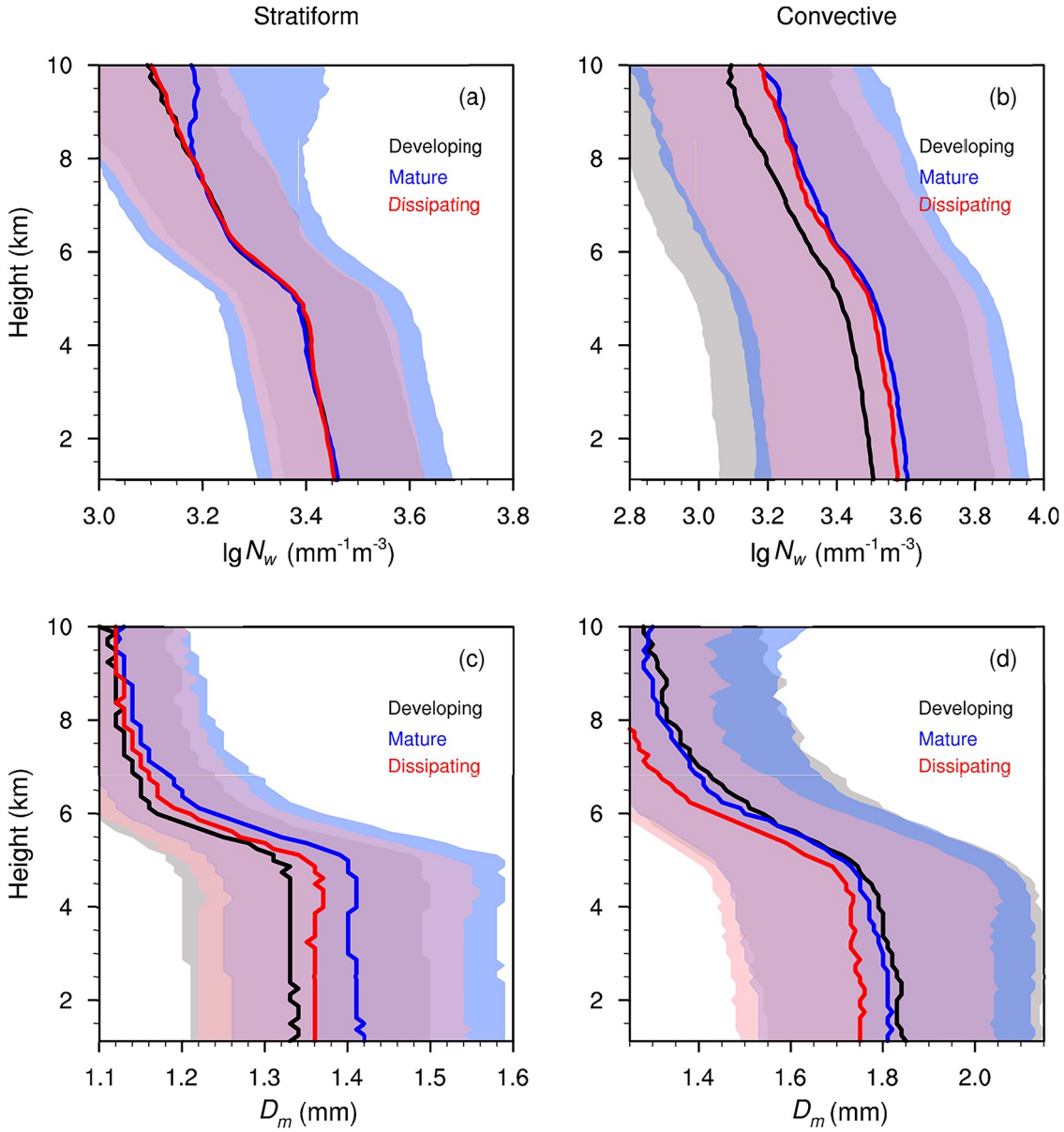

Fig. 14. Three stages of median lgN_w (a–b) and D_m (c–d) profiles (thick lines) for (a, c) stratiform and (b, d) convective rain of the mei-yu precipitation systems derived from the GPM 2ADPR product during the period 2016–18. Shaded areas show the interquartile range [reproduced from Sun et al. (2020)].

two new surface sites. The Jingzhou site is about 100 km east of Yichang airport and has much less air traffic. The Xiangyang site is located at 200 km north of the Jingzhou site. The ground-based instruments at these two new sites are almost identical to those at the Xianning site during IMFRE-I. With these new sites, as well as the existing Xianning site and other surface sites in the lower reaches, we have now conducted phase two of IMFRE (IMFRE-II) over the middle and lower reaches of the YHRV, during June–July 2020 (Cui et al., 2020a). During IMFRE-II, we mainly focused on the Jingzhou surface site with aircraft in-situ measurements there. The S-band and X-band operational radars provided additional ground-based observations for mei-yu frontal systems over the middle reaches of the YHRV. The surface sites in the lower reaches of the YHRV included the Shouxian and Hefei sites of Anhui Province and the Nanjing (Jiangning) site of Jiangsu Province. These three surface sites consist of mostly the same instruments as those over the middle reaches, which provide detailed ground-based observations there.

The IMFRE-II campaign during the 2020 mei-yu season has been completed, and more details are provided in Cui et al. (2020a). The KA350 aircraft, based at Yichang airport, participated in IMFRE-II and flew ~17 hours during the period 16 June to 5 July, with a total of seven flights over the Jingzhou surface site. The 2020 mei-yu season was an abnormal mei-yu season with the following characteristics: (1) The entry date was 8 June, which is about 10 days

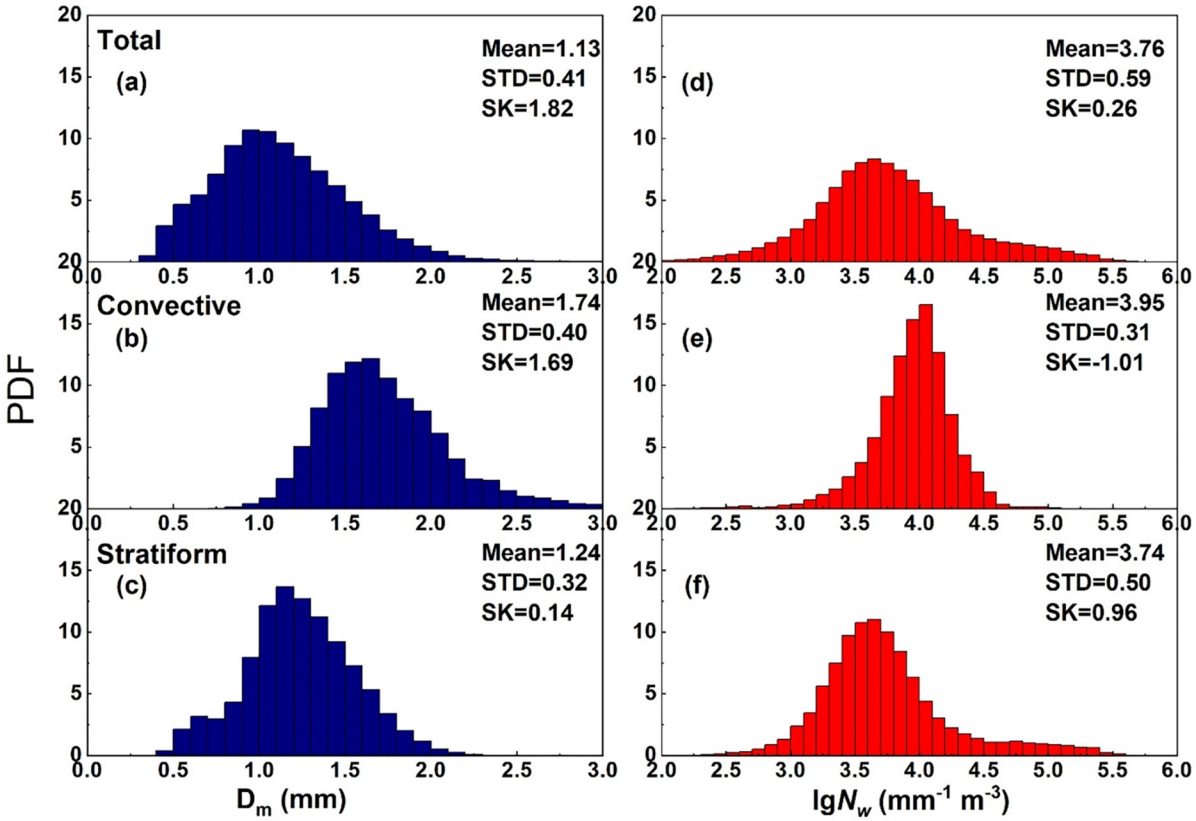

Fig. 15. Histograms of D_m and lgN_w for (a, d) all samples (106 544), (b, e) CR (6021), and (c, f) SR (31 876) during the 2016–18 mei-yu seasons, with mean values, standard deviations (STD), and skewnesses (SK) [reproduced from Fu et al. (2020)].

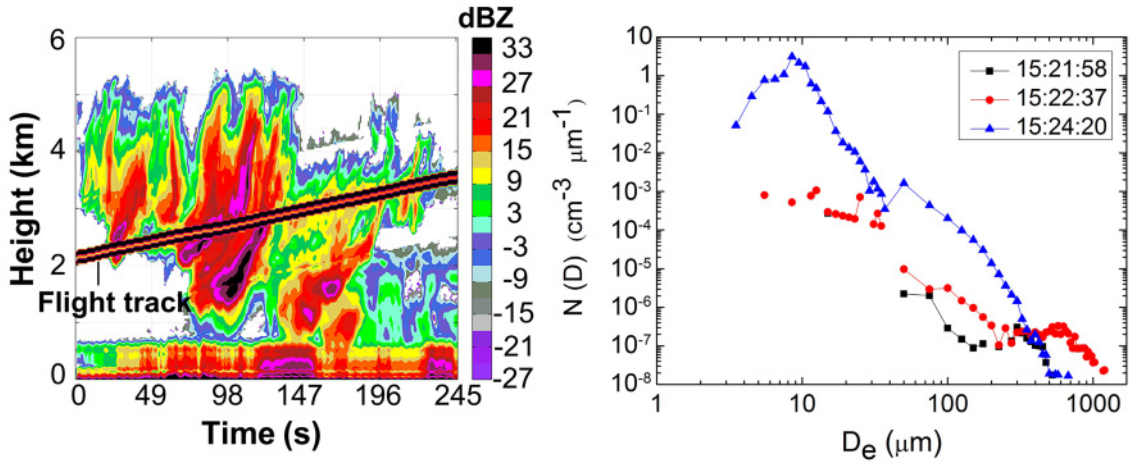

Fig. 16. (a) Ka-band (35.64 GHz) cloud radar reflectivity onboard the KingAir aircraft on 19 June 2018 during IMFRE-I. The flight track was from 1521:09 LST to 1525:14 LST and labeled every 49 seconds on the time axis. (b) Cloud and drizzle particle size distributions at top (blue), center (red) and bottom (black) of the cloud layer observed by the merged product from CDP (2–50 μm), CIP (25–1550 μm) and PIP (100–6200 μm), respectively.

earlier than normal, while the end date was 21 July, which is also later than normal. Thus, the entire mei-yu season was 44 days, which is 10 days more than normal. (2) There were a total of 10 mei-yu frontal systems during the 2020 mei-yu season, which is much more than normal. (3) In addition to more precipitation events, their precipitation rates and coverages were also much stronger and larger than the normal, and some regions with the historical record of rainfall. (4) The precipitation systems were steadily located around the YHRV with minor meridional fluctuations, which resulted in severe flooding over the middle and lower reaches of the YHRV.

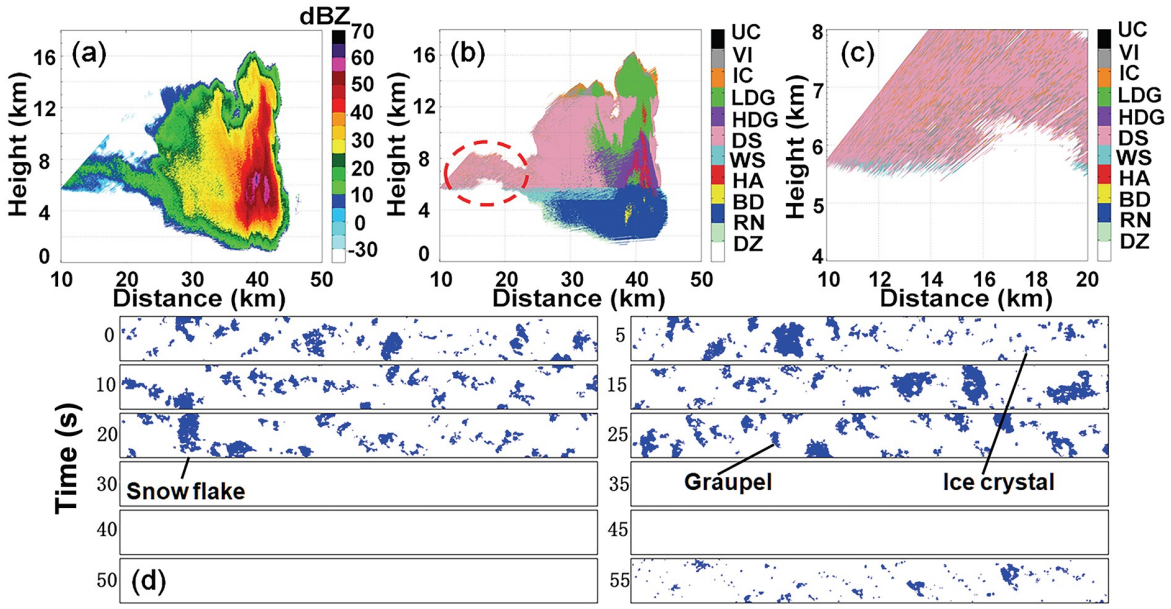

Fig. 17. Composite images of the (a) range height indicator (RHI) of IHR C-POL radar reflectivity and (b) hydrometeor categories, with (c) showing enlarged hydrometeor categories in the area of the red dashed oval in (b). The radar RHI scanning azimuth is 350° at 1729 LST on 24 June 2018 (case 2). (d) Aircraft PIP images sampled every five seconds starting from 1739 LST.

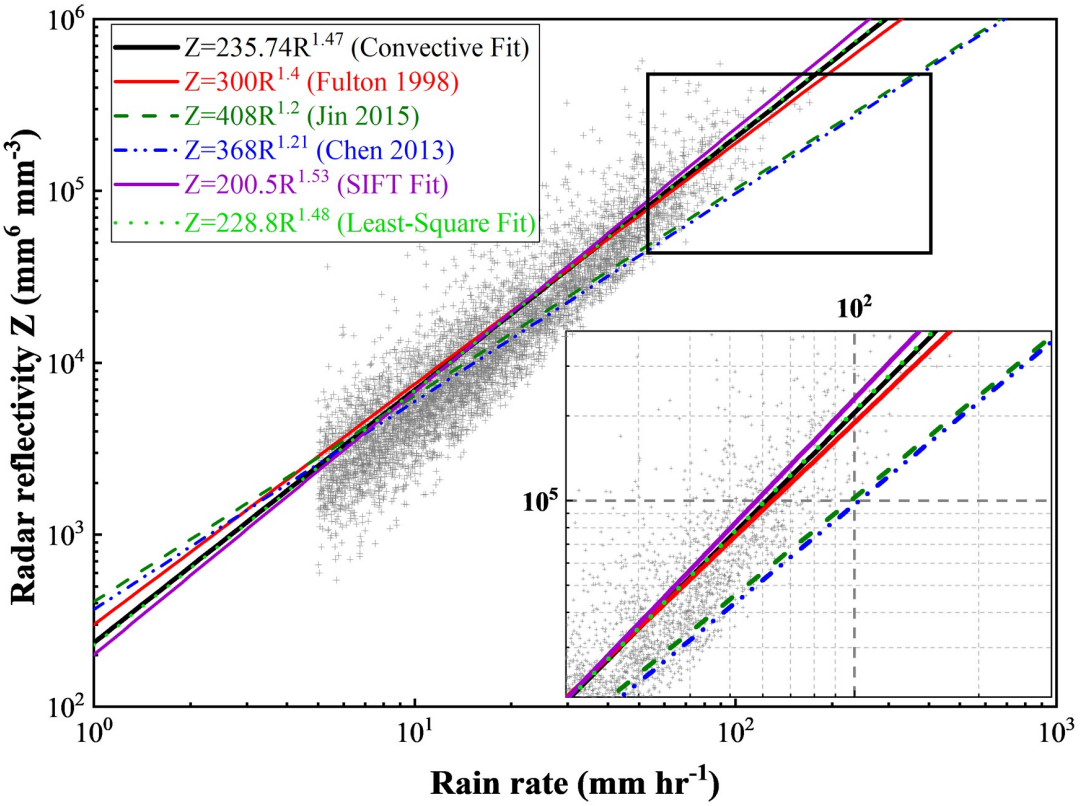

Fig. 18. Scatterplots of radar reflectivity (Z) and CR RR (gray crosses). The fitted power-law Z–R relationship for CR is shown by the black line. The red solid line represents the classic Z–R relationship derived from NEXRAD (Fulton et al., 1998), and the dark-green dashed line and double dot-dashed line represent the Z–R relationships derived from the results over Chuzhou and Nanjing. The purple solid line and light-green dotted line represent the Z–R relationship by the Sequential Intensity Filtering Technique (SIFT) and the least-squares method for all samples (CR, SR, mixed rain), respectively. The inset plot represents the amplified black rectangular region in the upper-right corner [reproduced from Fu et al. (2020)].

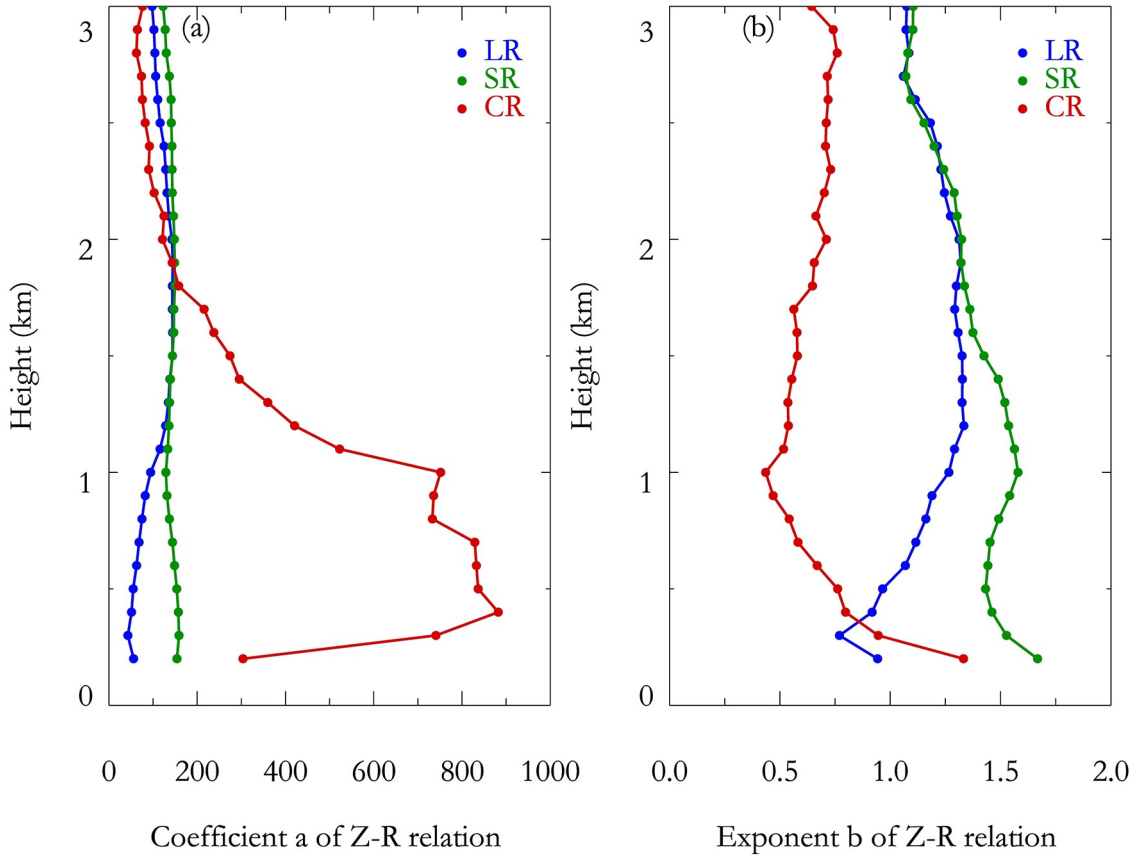

Fig. 19. Vertical profiles of the (a) coefficients and (b) exponents in the *Z*–*R* relationships ($Z = aR^b$) for classified LR, SR, and CR categories [reproduced from Zhou et al. (2020)].

The ground-based and satellite observations and aircraft in-situ measurements during IMFRE-II will help us further answer the three scientific questions posed for IMFRE. With a broader spatial coverage, the comprehensive datasets collected during IMFRE-II will allow better characterizations of the formation mechanisms and spatiotemporal evolutions of mei-yu frontal systems over the middle and lower reaches of the YHRV and the eventual establishment of a conceptual model of the multiscale systems inherent of mei-yu fronts. It will certainly benefit the investigation of the cloud and rain microphysical processes and properties, as well as cloud-to-rain particle conversion and growth processes, during mei-yu frontal rainfall. For example, for a two-layer cloud structure of a mei-yu rainband (e.g., Browning and Harrold, 1970; Takeda, 1971), the rain drops (and/or ice particles) fall from the upper parts of cumulus cloud and rapidly grow into large rain drops near the surface by collecting cloud droplets and small drizzle/rain drops through the collision–coalescence process. This well-known two-layer cloud model in the mei-yu system should be further studied in IMFRE-II as a basic rain-enhancing mechanism. These results will also enable more thorough modeling and data assimilation analyses that aim to constrain model microphysical/precipitation processes, especially parametric uncertainties, with new observations to achieve improved simulation and prediction of mei-yu rainfall storms, which pose considerable flooding threats to the lives and economic wellbeing of the people living in the YHRV.

Acknowledgements. The datasets were provided by the Mesoscale Heavy Rainfall Observing System (MHROS) of the Wuhan Institute of Heave Rain (IHR), China Meteorological Administration. The IMFRE field campaign is primarily supported by the National Natural Science Foundation of China (Grant Nos. 41620104009 and 91637211).

REFERENCES

Browning, K. A., and T. W. Harrold, 1970: Air motion and precipitation growth at a cold front. *Quart. J. Roy. Meteor. Soc.*, **96**, 369–389, https://doi.org/10.1002/qj.49709640903.

Chen, B., J. Yang, and J. Pu, 2013: Statistical characteristics of raindrop size distribution in the Meiyu season observed in eastern China. *Journal of the Meteorological Society of Japan Series II*, **91**(2), 215–227, https://doi.org/10.2151/jmsj.2013-208.

Chen, Y., and P. M. Zhai, 2014: Two types of typical circulation pattern for persistent extreme precipitation in Central-Eastern China. *Quart. J. Roy. Meteor. Soc.*, **140**(682), 1467–1478, https://doi.org/10.1002/qj.2231.

Chen, Y., and P. M. Zhai, 2016: Mechanisms for concurrent low-latitude circulation anomalies responsible for persistent extreme precipitation in the Yangtze river valley. *Climate Dyn.*, **47**(3), 989–1006, https://doi.org/10.1007/s00382-015-

2885-6.

Cui, C. G., and Coauthors, 2015: The Mesoscale Heavy Rainfall Observing System (MHROS) over the middle region of the Yangtze River in China. *J. Geophys. Res.*, **120**, 10 399–10 417, https://doi.org/10.1002/2015JD023341.

Cui, C. G., X. Q. Dong, B. Wang, and H. Yang, 2020a: The phase two of the integrative monsoon Frontal Rainfall Experiment (IMFRE-Ⅱ) in the middle and lower reaches of the Yangtze River in 2020. *Adv. Atmos. Sci.*, https://doi.org/10.1007/s00376-020-0262-9.

Cui, W. J., X. Q. Dong, B. K. Xi, and M. Liu, 2020b: Cloud and precipitation properties of MCSs along the Meiyu frontal zone in central and southern China and their associated large-scale environments. *J. Geophys. Res.*, **125**, e2019JD031601, https://doi.org/10.1029/2019JD031601.

Ding, Y. H., 1992: Summer monsoon rainfalls in China. *J. Meteor. Soc. Japan*, **70**(1B), 373–396, https://doi.org/10.2151/jmsj1965.70.1B_373.

Ding, Y. H., and J. C. L. Chan, 2005: The East Asian summer monsoon: An overview. *Meteorol. Atmos. Phys.*, **89**, 117–142, https://doi.org/10.1007/s00703-005-0125-z.

Ding, Y. H., J. J. Liu, Y. Sun, Y. J. Liu, J. H. He, and Y. F. Song, 2007: A study of the synoptic-climatology of the Meiyu system in East Asia. *Chinese Journal of Atmospheric Sciences*, **31**, 1082–1101, https://doi.org/10.3878/j.issn.1006-9895.2007.06.05. (in Chinese with English abstract)

Ding, Y. H., P. Liang, Y. J. Liu, and Y. C. Zhang, 2020: Multiscale variability of Meiyu and its prediction: A new review. *J. Geophys. Res.*, **125**, e2019JD031496, https://doi.org/10.1029/2019JD031496.

Fang S., K. Wang, M. Wang, and Z. Lv, 2019: Hubei Climate Service Handbook: Climate Background. Wuhan Regional Climate Centre (WRCC), 137 pp (in Chinese).

Fu, Z. K., X. Q. Dong, L. L. Zhou, W. J. Cui, J. Y. Wang, R. Wan, L. Leng, and B. K. Xi, 2020: Statistical characteristics of raindrop size distributions and parameters in central China during the Meiyu seasons. *J. Geophys. Res.*, **125**, e2019JD031954, https://doi.org/10.1029/2019JD031954.

Fulton, A., R. P. Breidenbach, D.-J. Seo, D. A. Miller, and T. O'Bannon, 1998: The WSR-88D rainfall algorithm. *Weather and Forecasting*, **13**, 377–395, https://doi.org/10.1175/1520-0434(1998)013<0377:TWRA>2.0.CO;2.

Geng, B., 2014: Case Study of a split front and associated precipitation during the Mei-Yu season. *Wea. Forecasting*, **29**, 996–1002, https://doi.org/10.1175/WAF-D-13-00111.1.

Geng, B., and H. Yamada, 2007: Diurnal variations of the Meiyu/Baiu rain belt. *SOLA*, **3**, 61–64, https://doi.org/10.2151/sola.2007-016.

Guan, P. Y., G. X. Chen, W. X. Zeng, and Q. Liu, 2020: Corridors of Mei-Yu-season rainfall over eastern China. *J. Climate*, **33**, 2603–2626, https://doi.org/10.1175/JCLI-D-19-0649.1.

Hu, Y., Y. Deng, Z. M. Zhou, C. G. Cui, and X. Q. Dong, 2019a: A statistical and dynamical characterization of large-scale circulation patterns associated with summer extreme precipitation over the middle reaches of Yangtze River. *Climate Dyn.*, **52**(9–10), 6213–6228, https://doi.org/10.1007/s00382-018-4501-z.

Hu, Y., Y. Deng, Z. M. Zhou, H. L. Li, C. G. Cui, and X. Q. Dong, 2019b: A synoptic assessment of the summer extreme rainfall over the middle reaches of Yangtze River in CMIP5 models. *Climate Dyn.*, **53**, 2133–2146, https://doi.org/10.1007/s00382-019-04803-3.

Jin, Q., Y. Yuan, H. J. Liu, C. E Shi, and J. B. Li, 2015: Analysis of microphysical characteristics of the raindrop spectrum over the area between the Yangtze River and the Huaihe River during summer. *Acta Meteorologica Sinica*, **73**(4), 778–788, https://doi.org/10.11676/qxxb2015.036.

Li, C., Y. Deng, C. G. Cui, X. F. Wang, X. Q. Dong, and X. W. Jiang, 2020: Hydrometeor budget of the Meiyu frontal rainstorms associated with two different atmospheric circulation patterns. *J. Geophys. Res.*, **125**, e2019JD031955, https://doi.org/10.1029/2019JD031955.

Lin, Y. J., R. W. Pasken, and H. W. Chang, 1992: The structure of a subtropical prefrontal convective rainband. Part I: Mesoscale kinematic structure determined from Dual-Doppler measurements. *Mon. Wea. Rev.*, **120**, 1816–1836, https://doi.org/10.1175/1520-0493(1992)120<1816:TSOASP>2.0.CO;2.

Liu, L., and Coauthors, 2020: Localization and invigoration of Mei‐Yu front rainfall due to aerosol‐cloud interactions: A preliminary assessment based on WRF simulations and IMFRE 2018 field observations. *J. Geophys. Res.*, **125**, e2019JD031952, https://doi.org/10.1029/2019JD031952.

Liu, M. L., and Q. Q. Wang, 2006: Anomalies of extreme precipitation during the Meiyu period of Jianghuai valleys and its general circulation characteristics. *Proceedings of 2006 Annual Meeting of the Chinese Meteorological Society*, Chinese Meteorological Society, Chengdu, China, 1899–1908. (in Chinese)

Luo, Y. L., Y. Gong, and D. L. Zhang, 2014: Initiation and organizational modes of an extreme-rain-producing mesoscale convective system along a Mei-Yu front in East China. *Mon. Wea. Rev.*, **142**, 203–221, https://doi.org/10.1175/MWR-D-13-00111.1.

Marshall, J. S., and W. M. K. Palmer, 1948: The distribution of raindrops with size. *Journal of Meteorology*, **5**(4), 165–166, https://doi.org/10.1175/1520-0469(1948)005%c0165:TDORWS%e2.0.CO;2.

Ninomiya, K., and K. Kurihara, 1987: Forecast experiment of a long-lived meso-α-scale convective system in Baiu frontal zone. *J. Meteor. Soc. Japan*, **65**, 885–899, https://doi.org/10.2151/jmsj1965.65.6_885.

Sampe, T., and S. P. Xie, 2010: Large-scale dynamics of the Meiyu-Baiu rainband: Environmental forcing by the westerly Jet. *J. Climate*, **23**, 113–134, https://doi.org/10.1175/2009JCLI3128.1.

Sun, Y. T., X. Q. Dong, W. J. Cui, Z. M. Zhou, Z. K. Fu, L. L. Zhou, Y. Deng, and C. G. Cui, 2020: Vertical structures of typical Meiyu precipitation events retrieved from GPM-DPR. *J. Geophys. Res.*, **125**, e2019jd031466, https://doi.org/10.1029/2019JD031466.

Takeda, T., 1971: Numerical simulation of a precipitating convective cloud: The formation of a "long-lasting" cloud. *J. Atmos. Sci.*, **28**(3), 350–376, https://doi.org/10.1175/1520-0469(1971)028<0350:NSOAPC>2.0.CO;2.

Tao, S. Y., and L. X. Chen, 1987: A review of recent research on the East Asian summer monsoon in China. *Monsoon Meteorology*, C. P. Chang and T. N. Krishnamurti, Eds., Oxford University Press, 60–92.

Wang, W. C., W. Gong, and H. L. Wei, 2000: A regional model simulation of the 1991 severe precipitation event over the Yangtze-Huai River valley. Part I: Precipitation and circulation statistics. *J. Climate*, **13**, 74–92, https://doi.org/10.1175/1520-0442(2000)013<0074:ARMSOT>2.0.CO;2.

Wang, X. K., X. Q. Dong, Y. Deng, C. G. Cui, R. Wan, and W. J. Cui, 2019: Contrasting pre-Mei-Yu and Mei-Yu extreme precipitation in the Yangtze River valley: Influencing systems and precipitation mechanisms. *Journal of Hydrometeorology*, **20**, 1961–1980, https://doi.org/10.1175/JHM-D-18-0240.1.

Yang, H., G. Y. Xu, C. G. Cui, J. Y. Wang, and D. X. He, 2019: Quantitative analysis of water vapor transport during Mei-Yu front rainstorm period over the Tibetan plateau and Yangtze-Huai River basin. *Advances in Meteorology*, **2019**, 6029027, https://doi.org/10.1155/2019/6029027.

Yang, J. M., and Coauthors, 2020: Spatial distribution and impacts of aerosols on clouds under Meiyu frontal weather background over central China based on aircraft observations. *J. Geophys. Res.*, **125**, e2019JD031915, https://doi.org/10.1029/2019JD031915.

Zhang, A. Q., Y. L. Chen, S. N. Zhou, C. G. Cui, R. Wan, and Y. F. Fu, 2020: Diurnal variation of Meiyu rainfall in the Yangtze plain during atypical Meiyu years. *J. Geophys. Res.*, **125**, e2019JD031742, https://doi.org/10.1029/2019JD031742.

Zhang, G. F., J. Z. Sun, and E. A. Brandes, 2006: Improving parameterization of rain microphysics with disdrometer and radar observations. *J. Atmos. Sci.*, **63**(4), 1273–1290, https://doi.org/10.1175/jas3680.1.

Zhang, S. L., S. Y. Tao, Q. Y. Zhang, and J. Wei, 2002: Large and meso-α scale characteristics of intense rainfall in the mid- and lower reaches of the Yangtze River. *Chinese Science Bulletin*, **47**, 779–786, https://doi.org/10.1360/02tb9176.

Zhang, X. L., S. Y. Tao, and S. L. Zhang, 2004: Three types of heavy rainstorms associated with the Meiyu front. *Chinese Journal of Atmospheric Sciences*, **28**, 187–205, https://doi.org/10.3878/j.issn.1006-9895.2004.02.03. (in Chinese with English abstract)

Zhou, L. L., X. Q. Dong, Z. K. Fu, B. Wang, L. Leng, B. K. Xi, and C. G. Cui, 2020: Vertical distributions of raindrops and Z-R relationships using microrain radar and 2-D-video distrometer measurements during the Integrative Monsoon Frontal Rainfall Experiment (IMFRE). *J. Geophys. Res.*, **125**, e2019JD031108, https://doi.org/10.1029/2019JD031108.